Applied Catalysis B: Environmental 329 (2023) 122532

Contents lists available at ScienceDirect

Applied Catalysis B: Environmental

journal homepage: www.elsevier.com/locate/apcatb

Crowded supported metal atoms on catalytically active supports may compromise intrinsic activity: A case study of dual-site Pt/α-MoC catalysts

Ewa Chukwu [a], Lindsay Molina [a], Conner Rapp [a], Luis Morales [a], Zehua Jin [a], Stavros Karakalos [b], Hui Wang [c], Sungsik Lee [d], Michael J. Zachman [e], Ming Yang [a,*]

[a] Department of Chemical and Biomolecular Engineering, Clemson University, Clemson, SC 29634, USA
[b] Department of Chemical Engineering, University of South Carolina, 301 Main Street, Columbia, SC 29208, USA
[c] Institute for New Energy Materials and Low Carbon Technologies, School of Materials Science and Engineering, Tianjin University of Technology, Tianjin 300884, China
[d] X-ray Science Division, Argonne National Laboratory, 9700 South Cass Avenue, Argonne, IL 60439, USA
[e] Center for Nanophase Materials Sciences, Oak Ridge National Laboratory, Oak Ridge, TN 37831, USA

ARTICLE INFO

Keywords:
Supported metal catalysts
Single-atom catalysis
Molybdenum carbide
Platinum
CO_2 conversion

ABSTRACT

Increasing the surface population of supported catalytic sites, assuming these sites are stable, is considered a straightforward approach to improving the overall catalytic performance. We report an exception represented by the Pt/α-MoC catalysts featuring atomically dispersed Pt. The Pt/α-MoC catalysts display very high activity for the reverse water gas shift reaction with near 100% CO selectivity for CO_2:H_2 ratios from 0.25 to 4 and from 250 to 400 °C. Despite the excellent performance, the intrinsic activity per Pt-centric catalytic center declines as the Pt loading increases from 0.1 to 1.0 wt%. With the dispersed Pt evolving from isolated atoms to fully exposed ensembles, the shrinking inter-Pt-atom space impedes CO_2 activation at the critical Pt-Mo interfaces, where the Pt shall temporarily take the -O intermediates. The Pt, even as atomically dispersed without noticeable sintering, is underutilized in such a crowded state. This caution for high-loading catalyst design is translational to other systems where the direct catalytic roles of the supports are crucial.

1. Introduction

Single-atom catalysts (SACs) maximize the utilization of the supported metals by stabilizing the latter as atomically dispersed species on catalyst supports [1–5]. Fundamentally, SACs bridge molecular catalysis with heterogenous catalysis by enabling a precise measure of the supported catalytic centers as individual metal atoms. In the pioneering SAC prototypes, support materials with limited or secondary catalytic roles were often adopted to better assist the unambiguous identification of structure-reactivity relationship focusing on the supported metal atoms [6–18]. Given that the intrinsic activity per supported metal atom stays constant and the structures are stable, the natural next development is to increase the loading of the supported metal atom and thereby improve the overall catalytic activity. Recently, outstanding SACs with high metal loadings $\geq$ 5 wt% have been developed [19–22].

However, in a pioneering model catalyst work by Goodman and co-workers [23], the authors made a rare finding that while the supported Pd monomer is indeed the catalytic center for ethylene acetoxylation on catalytically inert Au facets, the spacing between the noncontiguous Pd monomers would significantly impact the intrinsic activity per Pd site. What has been even less investigated is how the population density of the supported metal atoms will influence the catalysis when the supports are also catalytically active, a common case in many applied catalysis applications. These uncertainties pose an important question about how we shall more carefully leverage catalytically active supports and the supported metal atoms, as dual-site catalysts, to design better versions of supported metal catalysts, using high- and low-loadings of SACs as testing grounds.

In this work, we chose the single-atom Pt/α-MoC catalysts for the reverse water-gas shift reaction (RWGS) as our targeted system. The reaction is of industrial importance to mitigate CO_2 emissions, and involves rearrangements of -H, -CO, and -O radicals which are of broad relevance in many hydrogenation reactions. Acknowledging that the platinum group metals (PGMs) would often wrestle with the possible strong *CO adsorption during the CO_2 activation under RWGS conditions [24–26], we decided to adopt the Mo_xC as the representative catalytically active supports to provide an alternative space for CO_2 activation [27–32]. Due to the unique capability of Mo_xC to break the

* Corresponding author.
E-mail address: myang3@clemson.edu (M. Yang).

https://doi.org/10.1016/j.apcatb.2023.122532
Received 15 November 2022; Received in revised form 18 January 2023; Accepted 23 February 2023
Available online 27 February 2023

C═O bond in CO_2, the molybdenum carbides with quasi-platinum-metal chemical properties display promising RWGS activity [32]. According to theoretical studies, these carbides bind carbon-bound radicals weakly and thus would favor facile *CO desorption [33]. These desired $CO_2 \rightarrow CO$ chemistry from Mo_xC, in concert with the supported PGMs that generally have little to zero energy barriers for H_2 activation [18,34,35], warrant promises for RWGS.

The present work shows that, despite the outstanding performance of the catalysts, unexpectedly, the higher surface density of Pt atoms on α-MoC hinders their remarkable RWGS intrinsic activity. Unlike the previous work focusing on Pt nanoparticles for the different yet related water gas shift reaction, this "self-poisoning" of high Pt loading here is not due to the formation of sintered Pt particles or 2-dimensional Pt islands (largely metallic) [36], where only a fraction of the particles, such as the surface, perimeter, or corner atoms [37] are active. In our case, we find that the atomic Pt species is stable and remains dispersed after the RWGS. In this dual-site catalyst formulation, the activation of CO_2 and the subsequent desorption of *CO rely heavily on the MoC substrate and are substantially decoupled from the Pt atoms. However, a significant portion of the Pt atoms, presumably those in the interior of the crowded-Pt-atom areas (fully exposed Pt ensembles) covering the MoC substrates, becomes spectator species to take over the -O from CO_2 activation steps, thereby compromising the overall catalytic material efficiency.

2. Experimental

2.1. Catalysts synthesis

2.1.1. Preparation of MoO_3 nanorods

Ammonium molybdate (para) tetrahydrate (AMT, $(NH_4)_6Mo_7O_{24}{\cdot}4H_2O$, 81–83% as MoO_3) from Alfa Aesar was utilized for the preparation of MoO_3 nanorods by a modified hydrothermal treatment [28,38]. Briefly, 2.1 g of AMT was dissolved in a 60 mL mixed solution (5:1) of deionized water and > 62% HNO_3. The resulting solution was transferred into a Teflon-lined stainless-steel autoclave and heated in a furnace (Lindberg Blue M) at 200 °C for 20 h and thereafter cooled down to room temperature. The product was recovered by centrifugation, washed alternately with deionized water and ethanol, dried overnight at 60 °C, and then crushed. The crushed particles were calcined for 4 h at 500 °C with a 10 °C/min ramping rate.

2.1.2. Preparation of α-MoC nanorods

1 g of MoO_3 nanorod powder was loaded in the tubular quartz reactor, held with quartz wool at both ends, and placed in a horizontal furnace (Lindberg Blue M). The MoO_3 nanorod powder was heated in 125 mL/min of ammonia to 700 °C at 5 °C/min. The reactor was soaked at 700 °C for 2 h and then cooled down in argon to room temperature and the gas was switched to 20% CH_4/H_2, ramped to 700 °C at 5 °C/min and soaked for 2 h before cooling down in Ar to room temperature. The resulting powder α-MoC nanorods were passivated using 1% O_2/Ar for 12 h.

2.1.3. Preparation of α-MoC-nanorods-supported Pt catalysts

Pt/α-MoC catalysts of varying Pt loadings (0.1–1.0 wt%) were prepared via temperature-programmed carburization. Briefly, for a given Pt loading, MoO_3 nanorods were introduced into the desired concentration of tetraammineplatinum (II) precursor (purchased from Alfa Aesar) in deionized water, well stirred, dried at 110 °C for 3 h, and crushed. The resulting Pt/MoO_3 was calcined in air at 500 °C for 4 h (ramping rate 10 °C/min). The calcined Pt/MoO_3 powder was subjected to a two-stage temperature-programmed carburization in 125 mL/min of 20% CH_4/H_2 gas at 700 °C (ramped up from room temperature to 300 °C at 5 °C/min, then ramped to 700 °C at 1 °C/min and soaked for 2 h in the 20% CH_4/H_2 atmosphere. After carburization, the gas feed stream was switched to Argon and the sample was cooled down to room temperature and passivated with 25 mL/min of 1% O_2/Ar gas mixture for 12 h.

2.1.4. Preparation of benchmark catalysts

The desired concentration of tetraammineplatinum (II) precursor was incorporated onto the commercial ceria support (~ 50 m^2/g) by incipient wet impregnation, dried at 110 °C for 1 h and then crushed. The resulting sample was calcined in air at 550 °C for 2 h (ramping rate of 5 °C/min) and cooled down to room temperature after calcination. 0.5 wt% Pt/TiO_2 was also prepared with a similar procedure. The Pt/TiO_2 sample was prepared using ≥ 300 m^2/g TiO_2 support (TRONOX). The benchmark catalysts were treated with 50 mL/min 10% H_2/Ar at 250 °C for 30 min prior to catalytic tests.

2.2. Evaluation of catalytic performance

Catalysts were tested in a fixed-bed tubular quartz reactor at atmospheric pressure. 50 mg of catalyst diluted with 180 mg of quartz sand was loaded and supported on quartz wool in the reactor. Prior to reaction test, the catalyst sample was pretreated with 25 mL/min of 20% CH_4/H_2 gas mixture at 400 °C (10 °C/min heating rate) for 2 h and cooled down to the initial temperature 250 °C. The benchmark catalysts (Pt/CeO_2 and Pt/TiO_2) were mildly reduced with 50 mL/min 10% H_2/Ar at 250 °C for 30 min

Unless otherwise stated, pretreated catalysts were purged with Ar and exposed to 100 mL/min of reactant gas (10% CO_2, 20% H_2 and 70% Ar) and the reaction was performed between 250 and 400 °C. Reaction products were monitored with an MKS Series 2000 MultiGas Analyzer. Steady-state reaction data were collected after 20 min of reaction

$$CO_2\ conversion, X\ (\%) = \frac{n_{CO} + n_{CH_4}}{n_{CO_{2_{in}}}} 100$$

$$CO\ selectivity,\ S\ (\%) = \frac{n_{CO}}{n_{CO} + n_{CH_4}} 100$$

$$\text{Carbon balance(CB)was computed with}: \frac{n_{CO_{2_{out}}} + n_{CO} + n_{CH_4}}{n_{CO_{2_{in}}}} \times 100$$

$n_{CO_{2_{out}}}, n_{CO}$, and n_{CH_4} are the molar flowrates of CO_2, CO, and CH_4 in the reactor output respectively while $n_{CO_{2_{in}}}$ is the molar flowrate of CO_2 in the feed stream.

Carbon balances were ~ 100%.

2.2.1. Kinetic measurements

Kinetic data were all obtained under the kinetic regimes by adjusting the GHSV between 400,000 to 660,000 mL/g_{cat}.h using 10–15 mg of catalysts diluted with 30 mg quartz sand (catalyst bed height ~ 4 mm). With a temperature range of 250–310 °C, CO_2 conversions were consistently below 10% for all tested samples at all temperatures. To further eliminate possible artifacts resulting from equilibrium effects (minor) due to the reversible reaction, the corresponding forward RWGS reaction rates were then obtained from the net reaction data using the approach-to-equilibrium parameter analysis.

$$\text{Net reaction rate}, r_f = r_n/(1-\beta) \quad (1)$$

r_n and r_f are the measured (net) and the computed forward reaction rates respectively.

β is the approach-to-equilibrium parameter, ranging from 0 to 1 as the reaction approaches equilibrium.

For our probe reaction,

$$\beta = P_{CO}P_{H_2O}/K_{eq}P_{CO_2}P_{H_2} \quad (2)$$

P_j is the average partial pressure of the gas.

K_{eq} is the equilibrium constant for reverse water gas shift reaction (varied according to our reaction temperature). For our catalytic reaction systems, β varied from 0.0013 to 0.061.

Consequently, the rate orders, apparent activation energy and intrinsic activity analyses were based on the forward reaction rates. Turnover Frequencies (TOFs) were based on the nominal Pt loadings (assuming 100% Pt metal dispersion and full accessibility by the reactants) rather than "accessible surface Pt" typically obtained by estimating the dispersion of the supported metal via CO/H_2 chemisorption techniques. Chemisorption techniques are difficult to apply to our system because 1) the Pt, unexpectedly, binds CO weakly even at ambient temperature, and 2) H_2 tends to be dissociated and spilled over to the carbide supports afterwards. Therefore, accurate counts of a fixed number of probe molecules per Pt atom can hardly be concluded. Consequently, the turnover frequency per mole Pt for our catalysts was based on the nominal Pt loading (which agrees with the actual Pt loading determined via ICP, see 1.3.3 below).

Rate orders for CO_2 and H_2 were obtained by fitting our experimental reaction data to the forward reaction power rate law equation below given that no RWGS products exist in the reaction feed stream:

$$forward reaction rate = kP_{CO_2}^{\alpha} P_{H_2}^{\beta}$$

2.2.2. Stability tests

Using 0.1Pt/α-MoC and 0.5Pt/α-MoC as representatives for our Pt/α-MoC catalysts, stability studies were conducted under kinetic control regimes using 100 mL of feed gas (10 mL/min CO_2, 10 mL/min H_2 and 80 mL/min Ar, 400,000 mL/g_{cat}.h). The catalyst sample was exposed to reactant gas mixture at 250 °C for 16 h.

2.3. Catalysts structural characterizations

2.3.1. Powder X-ray diffraction (XRD)

X-ray diffraction patterns of the samples were acquired using a Rigaku diffractometer (Ultima IV) equipped with Cu Kα radiation.

2.3.2. Brunauer-Emmett-Teller (BET) surface areas

BET surface area measurements for the samples were performed by N_2 physisorption at 77 K on Autosorb iQ Station2 instrument of the Advanced Materials Research Laboratory, Clemson University. Prior to N_2 adsorption, the samples were degassed at 300 °C under vacuum for 3 h. The specific surface areas for all catalysts were determined to be ~ 20 m^2/g.

2.3.3. Inductive coupled plasma optical emission spectroscopy (ICP-OES) analysis

The Pt loadings and Tungsten impurities (inherent in the MoC precursor) in our catalysts were quantified using a Thermo Fisher, iCAP 7200 ICP-OES Analyzer. For example, the actual Pt loadings measured by ICP are 0.095 and 0.487 wt% for 0.1Pt/α-MoC and 0.5Pt/α-MoC respectively, which are used for our TOFs computations.

2.3.4. Diffuse reflectance infrared Fourier transform spectroscopy (DRIFTS)

DRIFTS experiments were executed using a Nicolet iS50 FTIR equipped with a liquid N_2-cooled MCT detector. For the CO-DRIFTS, about 13 mg catalyst was loaded into the water-cooled-reaction chamber from Harrick Praying Mantis situated in the FTIR sample compartment. The catalyst was activated with 10 mL/min of 20% CH_4/H_2 gas mixture and cooled down in Ar to 25 °C and continuously purged with Ar for 1 h. After temperature stabilization, the background spectrum was collected by averaging 32 consecutive scans at 4 cm^{-1} resolution with the OMNIC Basic Macro programs. Next, CO gas was admitted (100 mL/min 15% CO/Ar) for 20 min, and sample spectra were collected. Each spectrum was an average of 16 consecutive scans and was processed with the OMNIC software. CO-DRIFTS was also performed for KBr at the same conditions. The KBr spectra served as the subtrahend for the removal of the gaseous CO contribution from the catalyst samples' spectra, where the adsorptions of carbonyl species are weak for these catalysts in general. For the CO-DRIFTS on α-MoC, CO adsorptions were also executed at 100, 150 and 200 °C following the exact procedure for the adsorption at 25 °C. CO_2-alone DRIFTS at various temperatures were conducted with 20 mL CO_2 and 70 mL Ar following the procedures for catalyst activation, data collection, and processing described above.

2.3.5. Aberration-corrected high-angle annular dark field scanning transmission microscopy (ac-HAADF-STEM)

The ac-HAADF-STEM images for our representative as-synthesized samples were acquired using FEI Titan Themis Cubed G2 60–300. The ac-HAADF STEM images acquired for the post-reaction sample (0.5Pt/α-MoC) obtained after 8 h of reaction under our stability test conditions (see section 1.2.2) were performed on an aberration-corrected Nion UltraSTEM 100 instrument, which was operated with an accelerating voltage of 100 kV and a convergence angle of ~32 mrad. The assignment of possible elements and compositions was probed by energy dispersive spectrometry (EDS) and STEM imaging contrast measurement proportional to the power of ~ 1.7 of the specific atomic numbers.

2.3.6. In-situ X-ray photoelectron spectroscopy (XPS)

The surface electronic environments of our representative catalysts were investigated with the AXIS Ultra DLD XPS (Kratos Analytical) instrument. The XPS system is equipped with a monochromatic Al Kα source operated at 15 keV and 150 W, a hemispherical analyzer, a charge neutralizer, a catalysis cell, and a load lock chamber for rapid introduction of samples without breaking vacuum. The X-rays were incident at an angle of 45°, with respect to the surface normal. Analysis was performed at a pressure of $\sim 1 \times 10^{-9}$ mbar and high-resolution core level spectra were measured with a pass energy of 40 eV. The XPS experiments were performed by using an electron beam, directed at the sample, for charge neutralization. The sample was loaded into the reaction cell (Model: ES-009R01) directly attached to the XPS chamber, which allows the samples to be transferred between the reaction and the XPS analysis chambers without exposure to the atmosphere. The loaded passivated catalyst was activated at 400 °C for 2 h using 10 mL/min 20% CH_4/H_2 gas mixture. After activation, the catalyst was purged and cooled to room temperature and transferred to the XPS chamber for measurements. The curve fitting procedure was carried out using the XPS Peak 41 software, and the peak approximation was carried out by a combination of Gaussian-Lorentzian functions, with subtraction of Shirley-type background.

2.3.7. X-ray absorption near edge structure (XANES)

XANES measurements of our representative samples were performed in fluorescence mode at the 12-BM of the Advanced Photon Source at Argonne National Laboratory. Passivated samples were activated and cooled down to ambient temperature. The Pt *L3* edge (11.564 keV) spectra were acquired. Five consecutive scans were executed per data collection point. The spectra for Pt foil and Pt(II) acetylacetonate were similarly collected to serve as Pt(0) and Pt(II) references respectively. The XANES spectra were processed with Athena software. We were unable to carry out the EXAFS analyses for Pt *L3* edge due to the contamination of W from ammonium molybdate tetrahydrate precursors acquired through Alfar Aesar and Sigma Aldrich companies in North America in the Fall 2020 to Summer 2022 timeframe. More detailed discussions are included in the later sections of the main text (Section 3.3).

2.4. Studies under reaction-relevant conditions

2.4.1. RWGS-DRIFTS

The RWGS-DRIFTS experiments under relevant reaction conditions were performed between 250 and 350 °C. Pretreatment of catalyst followed the same protocol as the aforementioned CO-DRIFTS experiments. About 13 mg passivated sample was activated with 10 mL/min of

20% CH_4/H_2 and cooled down to room temperature in Ar. After temperature stabilization and background spectra collection, the reaction cell temperature was ramped at 10 °C/min and stabilized at the targeted temperatures in flowing Ar. RWGS was performed with a 100 mL reactant gas mixture of 10 mL CO_2, 20 mL H_2 and balanced by the pre-existing Ar flow. Spectra were collected during the 20 min of reaction.

2.4.2. CO/H_2 reactor pulse experiments

15 mg sample diluted with 30 mg quartz sand was loaded into the reactor, activated with 10 mL/min of 20% CH_4/H_2 and cooled down in Ar to 250 °C. For a CO-preadsorbed sample test, 5 mL/min CO was admitted to the activated sample in Ar (net flow rate of 85 mL/min CO/Ar). After ~ 10 min of CO/Ar flow, 15 mL/min H_2 was introduced (net flow rate 100 mL/min CO+H_2/Ar). Reactor output was monitored with MKS Series 2000 MultiGas Analyzer. A similar experiment was performed with an H_2-preadsorbed sample. The activated catalyst in Ar was exposed to 15 mL/min H_2 for ~ 10 min before 5 mL/min CO was admitted (net flowrate 100 mL/min CO/H_2/Ar).

2.4.3. RWGS in-situ XPS

experiment. XPS instrument, operation, and pretreatment were exactly as previously described (vide infra). The activated and purged sample in the reaction chamber was exposed to 30 mL/min (10% CO_2, 20% H_2 and 70% Ar) at 250 °C for 20 min. After the reaction, the sample was transferred to the XPS chamber and measurements were executed at room temperature.

3. Results and discussion

3.1. α-MoC-supported Pt catalysts show superior RWGS performance

The α-MoC nanorods-supported Pt catalysts (0.1–1.0 wt% Pt/α-MoC), where the α-MoC nanorod retains a high aspect ratio (Figs. 1a and 1b and S1, $S_{BET} = 20\ m^2/g$) with a dominant (111) phase (Fig. 1c) to anchor Pt were synthesized. All diffraction peaks in the X-ray diffraction (XRD) results (Fig. 1c) for the Pt/α-MoC catalysts are indexed to the face cubic phase molybdenum carbide. The absence of any Pt peaks indicates that the Pt species are highly dispersed or below the detection limit of the XRD. Additionally, no oxide phase of molybdenum is observed in the XRD patterns, confirming complete carburization during synthesis and that the passivation at ambient temperatures after synthesis was only superficial and did not cause deep oxidation of the MoC [39].

The activated catalysts were subjected to RWGS reaction between 250 and 400 °C at atmospheric pressure. Fig. 2a shows that overall Pt/α-MoC catalysts are highly active for low-temperature RWGS, easily reaching equilibrium conversions above 250 °C under high gas-hourly-space-velocity (120,000 mL/g_{cat}.h) while maintaining ~ 100% CO selectivity across all investigated temperatures (Fig. 2b). These Pt/α-MoC catalysts, regardless of their Pt loadings, rank among the most active RWGS catalysts reported in the literature (Table S1). In comparison, the Pt/CeO_2 and Pt/TiO_2 reference catalysts show inferior activities below 300 °C and even lag the Pt-free MoC. Previous studies report that CO_2 binds on the Mo_xC surface in a bent configuration and undergoes direct C═O scission [40,41]. This bent geometry promotes electron transfer towards CO_2, which is critical for CO_2 adsorption and activation [42]. These results suggest that α-MoC, as catalyst support, plays a significant catalytic role in promoting the RWGS reaction.

3.2. Intrinsic activity of the Pt-centric reaction center declines as Pt loading increases

The intrinsic activity (turnover frequency, TOF) of the supported platinum species was measured under the kinetic regime by adjusting the gas hourly specific velocity (Fig. S2) and diluting catalysts with quartz sand. We acknowledge that for reversible reactions, reaction data can be compromised by the backward reaction because of approaching RWGS equilibriums. Hence, in addition to obtaining the reaction data under the kinetic control regime, only the forward reaction rates (RWGS) were utilized for all kinetic analyses (see experimental Section 2.2.1). Further, we note that typically, the dispersion of the Pt would be obtained via CO/H_2 chemisorption techniques. But chemisorption techniques are practically difficult for our system because 1) the Pt, unexpectedly, binds CO weakly even at ambient temperature, and 2) H_2 tends to be dissociated and spilled over to the carbide supports afterward. Therefore, an accurate assessment of Pt dispersion can hardly be concluded. The presence of Pt as an atomically dispersed species was suggested by electron microscopy, CO-DRIFTS, and X-ray characterizations (to be discussed later), so we tentatively evaluated the turnover

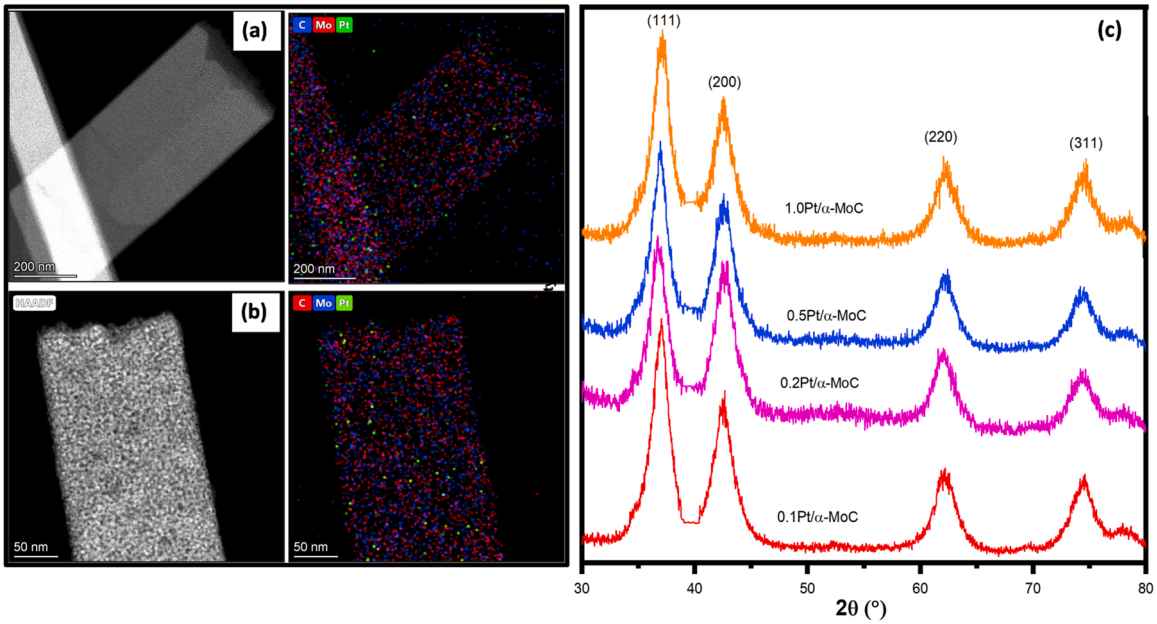

Fig. 1. Pt/α-MoC nanorod catalysts with highly dispersed Pt species: (a) HAADF-STEM and EDS images of 0.1 Pt/α-MoC, (b) HAADF-STEM and EDS images of 0.5 Pt/α-MoC, and (c) XRD patterns for the Pt/α-MoC catalysts.

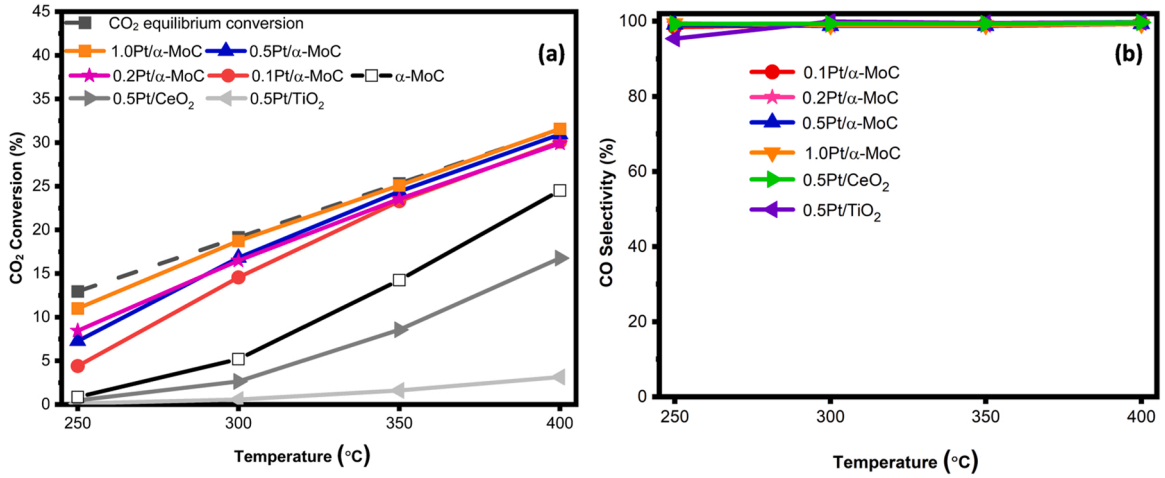

Fig. 2. RWGS catalytic performance as a function of temperature: (a) CO_2 conversions and (b) CO selectivity.All measurements were done using 50 mg of catalysts diluted with 180 mg of quartz, 100 mL of reactant feed of 10% CO_2, 20% H_2 and 70% Ar.

frequency (TOF) per mole of Pt, meaning each Pt atom anchoring on the α-MoC surfaces.

As shown in Fig. 3a, the TOFs declined aggressively as the surface Pt population increased from 0.1 to 0.5 wt%. Although the restructuring of the supported single-atom species into clusters under reaction conditions to shape the catalysis has been common [43,44], it is of a much lower likelihood for the Pt/Mo_xC system in general [45–48] and in this work. The atomically dispersed Pt stabilized by the Pt-Mo bonds [48] is stable under this reaction condition, as indicated by the stable reactivity data in the kinetic control regime (Figs. 3b and 3c) and intact identity of atomically dispersed Pt species after the reaction (Fig. S3). Therefore, the observed TOF trend does not derive from catalyst deactivation (SI-T1).

To explore the origin of the shifting/declining TOFs, we computed the apparent activation energies (E_{app}) for these catalysts (Fig. 4a). The E_{app} dropped as the Pt population density increased. The trends of E_{app} and TOFs together indicate that 0.1Pt/α-MoC and 0.5Pt/α-MoC are likely the threshold samples worthy of detailed comparisons. We observed a linear correlation between the pre-exponential factors and E_{app} (Fig. S4). This correlation, called the enthalpy-entropy compensation effect, hints that the activation energy pattern stems from entropic effects without altering the overall reaction pathways [49–51]. Guided by these implications, and by simplifying the RWGS as a single-step reaction to allow Eyring plot analyses (Fig. 4b), we found that the reaction entropies became more negative with increased Pt site population (- 236 kJ $mol^{-1}K^{-1}$ for 0.1Pt/α-MoC; - 251 kJ $mol^{-1}K^{-1}$ for 0.5Pt/α-MoC). The increase in the negative value of the entropy suggests a greater loss of a degree of freedom, and tighter confinement of reactants and transition states [50–52]. These results suggest that the increased Pt loading, even as highly-dispersed species, is not necessarily adding the same type of Pt-Mo catalytic center.

3.3. *Surface density of the Pt species does not impact the intrinsic structural properties of the Pt- Mo moieties*

To gain insights into the possible impact of Pt loading on the Pt-Mo moieties, we examined various structural and chemical properties of the Pt/α-MoC catalysts. The similarity in XRD patterns (Fig. 1c) and the X-ray photoelectron spectra (XPS) of the Mo *3d* (Fig. S5) for the down-selected 0.1Pt/α-MoC and 0.5Pt/α-MoC samples indicates that the α-MoC bulk structure remains essentially the same regardless of Pt loadings. Since the molybdenum carbide did not show any appreciable changes, to interrogate how the Pt-Mo catalytic center evolves with the increasing Pt surface population, we focused on the Pt. The Pt species in the down-selected 0.1Pt/α-MoC and 0.5Pt/α-MoC samples were then further characterized.

The visual structural identity of the Pt species was probed with ac-HAADF-STEM. We used an intentionally prepared 5Pt/α-MoC sample (Fig. S6, with 5 wt% Pt loading) to illustrate the presence of Pt nanoparticles ranging from 2 to 100 nm. However, such Pt species could

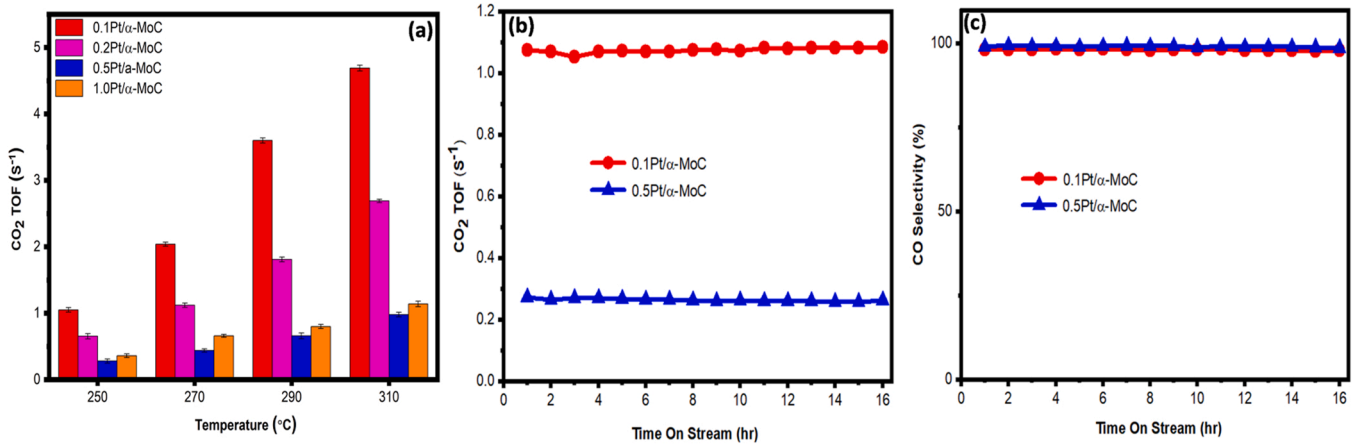

Fig. 3. RWGS catalytic performances of the Pt/α-MoC catalysts under the kinetic regime: (a) forward TOF per mole Pt as a function of temperature, and stable reactivity at 250 °C under 100 mL of reactant feed of 10% CO_2, 10% H_2 and 70% Ar. (b) forward TOF per mole Pt and (c) CO selectivity.

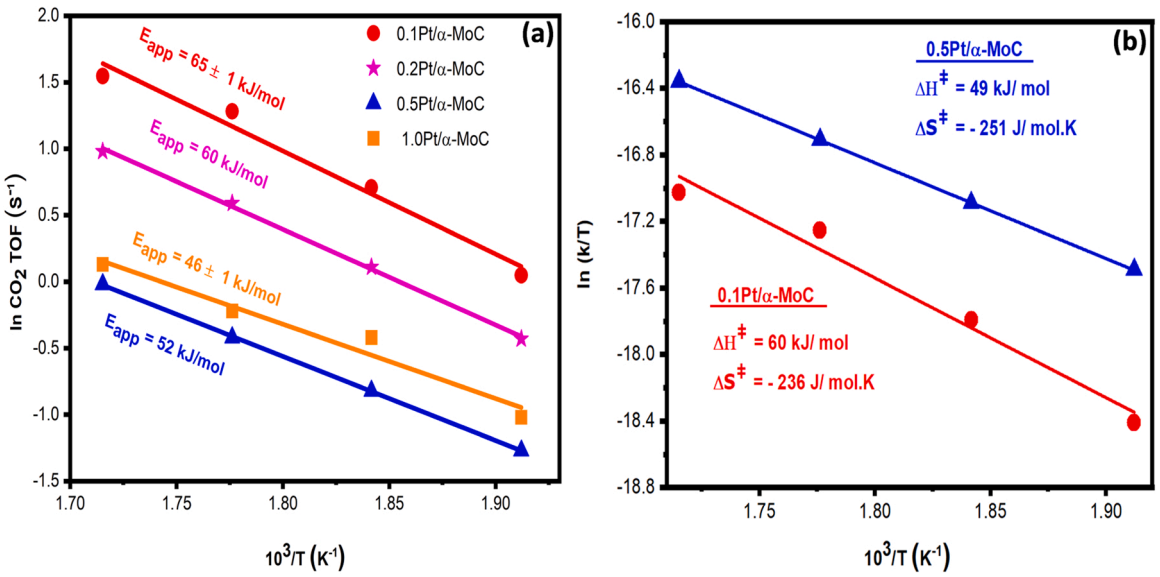

Fig. 4. Key apparent parameters for the Pt/α-MoC catalysts: (a) Arrhenius plots for apparent activation energy analyses (b) Eyring plots for estimating reaction enthalpy and entropy for the down-selected catalysts.

hardly be observed at low magnifications for the critical 0.1Pt/α-MoC and 0.5Pt/α-MoC samples (Fig. 1a and b), and the EDS results suggest the high dispersion of Pt at low contents in these two samples. At high magnifications, the ac-HAADF-STEM images for 0.1Pt/α-MoC (Fig. 5a-c) show that the Pt species are stabilized as isolated atoms on the MoC and generally well distanced from each other (highlighted with circles). Contrarily, while a few distantly isolated Pt atoms are still observable in 0.5Pt/α-MoC (Fig. 5d-f), the majority of Pt atoms become crowded in discrete areas as perhaps fully exposed Pt ensembles over the MoC substrate (highlighted with boxes). The circles and boxes only serve to

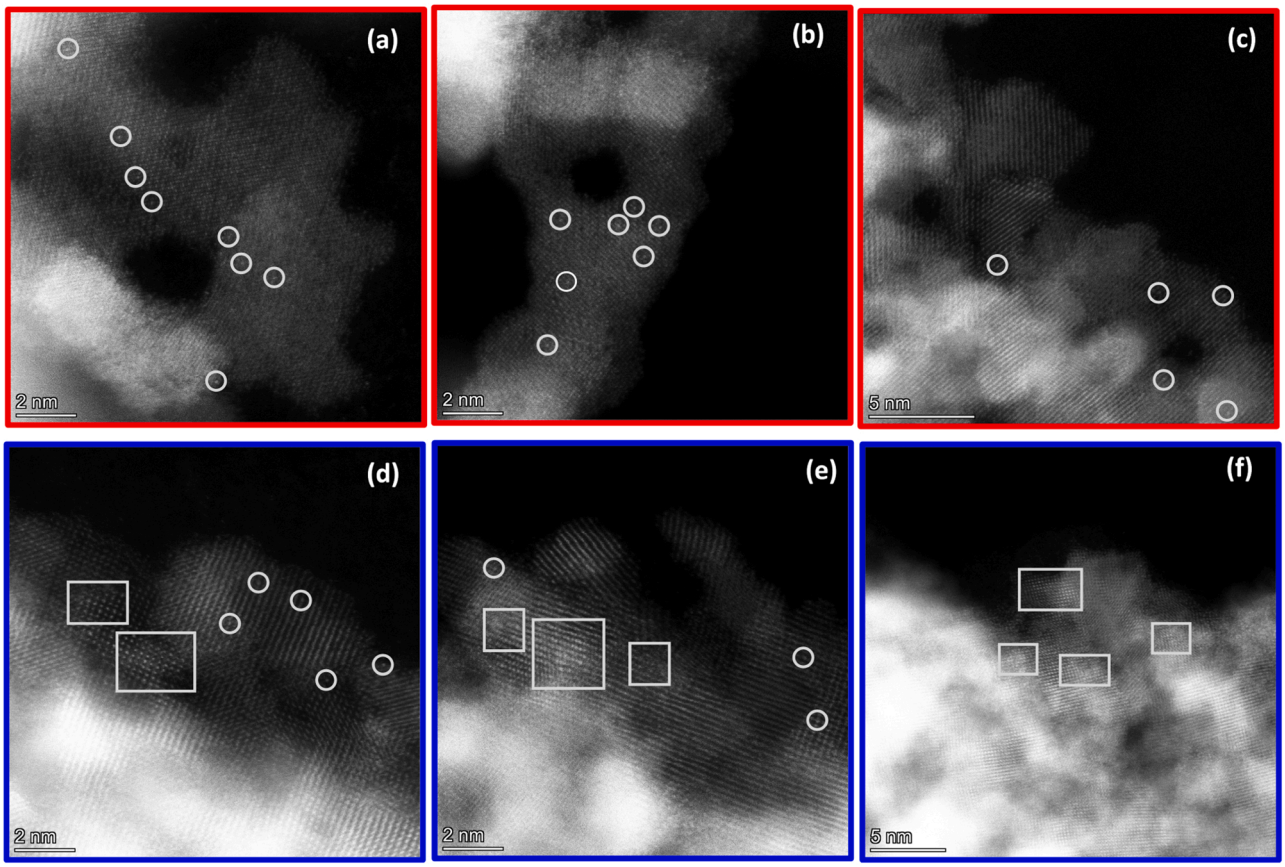

Fig. 5. ac-HAADF-STEM images of different edge areas for (a-c) 0.1Pt/α-MoC and (d-f) 0.5Pt/α-MoC. The circles highlight some of the isolated Pt atoms and the boxes are some of the fully exposed Pt ensembles areas over the MoC substrate. The circles and boxes only serve to point our readers to some of the locations of the isolated atoms and some of the areas containing the fully exposed ensembles respectively. The somewhat bright patches (~ ≥ 2 nm) existing in non-edge areas of the nanorod catalysts are due to the thick areas across the porous α-MoC substrate.

point to some of the locations of the isolated atoms and the areas containing the fully exposed ensembles respectively, in consistency with other recent works [53–59]. We want to caution that the somewhat bright patches (~ ≥ 2 nm) existing in almost every non-edge area of the α-MoC substrate originate from the thickness gradient across the α-MoC substrate surface due to its patterned porous nature (Figs. S7 and S8). Under the HAADF mode, by measuring the intensity of the bright areas against the less bright surroundings, the intensity ratio is noticeably less than the $(Z_{Pt}/Z_{Mo})^{1.7}$, suggesting the unlikelihood of the presence of Pt particles but dense and dilute regions of the α-MoC substrates. The lack of distinctive lattice patterns associated with metallic Pt particles further suggests the absence of Pt nanoparticles. Such bright patches are typical in recent pioneering literature studying the MoC-based catalysts, and similar bright patches observed were not considered as supported metal species with extended metal surfaces [46,48,60,61]. Admittedly, it was unclear up to this point whether the crowded Pt species in the fully exposed ensembles exhibit substantial Pt-x-Pt interactions as one would expect in typical Pt ensembles found by others [57,58] and ourselves [44]. Hence, to further characterize the Pt species, our STEM image finding was complemented by averaged techniques such as DRIFTS, XPS, and XANES oriented to surface, near surface, and bulk analyses respectively.

Intriguingly, the "visual" differences of the Pt species regarding catalyst surface coverage did not change the intrinsic chemistry of Pt. The samples were examined with CO-DRIFTS (Fig. 6). CO-DRIFTS can identify different atomic metal structures, like single-atoms, clusters, and nanoparticles, even as a function of electronic states [12,14,62,63]. In our work, the absence of typical carbonyl atop (2000–2060 cm^{-1}) and bridge bands (~ 1800–1950 cm^{-1}) suggests the absence of Pt nanoparticles [64–66]. The vibrational frequency of CO adsorbed on atomically dispersed Pt in the range of 2080–2135 cm^{-1} for Pt supported on metal oxide systems has been reported [13,44,67–69]. Hence, we note that ideally, the exact CO-Pt DRIFTS peaks would be captured after purging out the gaseous CO. However, even at 25 °C, CO molecules adsorbed weakly to our catalyst and disappeared after we switched from CO to Ar for 45 s (Fig. S9). Therefore, the CO gas phase was then subtracted with the CO-DRIFT spectra for KBr following the method proposed by Paredes-Nunez et al. [70]. Compared with the CO-DRIFTS for the pristine α-MoC (Fig. S10), we conclude that while CO can adsorb on the MoC [71,72], no detectable adsorbed CO on Pt in the Pt/α-MoC samples is observed (Fig. 6a and 6b). According to recent work [48], predicted CO adsorption energies on platinum nanoparticles, single-atom Pt on α-MoC, and bare α-MoC are - 2.59 eV, - 2.04 eV and - 2.28 eV respectively. This suggests that in the absence of Pt nanoparticles, the α-MoC would exhibit a stronger affinity for CO compared to the electron-deficient single-atom Pt species on α-MoC [46,48]. Hence for our Pt/α-MoC catalysts, in accordance with adsorption equilibrium (Langmuir adsorption isotherm), only a tiny amount of CO, below the sensitivity limit of DRIFTS, adsorbed on the single-atom Pt sites. This is attributed to the significantly weakened back-donation of electrons from the electron-deficient Pt *d* orbital to the CO anti-bonding orbital [46,48] as well as the additional competition created by the vast majority of the MoC surfaces for the more favorable CO adsorption. Our current work provides experimental proof for the computationally predicted CO adsorption trend on single-atom Pt/α-MoC system in a CO-only feed stream. Overall, the similarity in our CO-DRIFTS for 0.1 and 0.5Pt/α-MoC suggests that the Pt atoms possess similar structural and electronic properties that won't favor appreciable CO adsorptions.

In another effort, we employed in-situ X-ray photoelectron spectroscopy (XPS) to probe the electronic states of these Pt species in the as-prepared samples. Fig. 7a shows that the Pt species in the activated 0.1 and 0.5Pt/α-MoC catalysts have their Pt *4 f* peaks at ~ 71.6 eV with an FWHM of about 1.5 eV, in contrast to the 71.0 eV and the typically narrower FWHM around 1.0 eV for metallic Pt state [73]. When single-atom platinum is anchored on MoC, the Pt donates electrons to the MoC, resulting in electron-deficient Pt species and electron-rich Pt-Mo interfaces [45,46,48]. The X-ray absorption near-edge structure (XANES) spectra for the normalized Pt L_3 edges (Fig. 7b) for 0.1 and 0.5Pt/α-MoC are similar, with the absorption edge energy situated between those Pt^0 and Pt^{2+} references. This confirms that the Pt species in both samples possess a similar electron-deficient yet near-neutral state in agreement with the XPS analysis. The similarity in XANES spectra (Fig. 7b and 7c) for both catalysts indicates a high level of similarity in the chemical states and coordination environment of the Pt in both samples. Unfortunately, Tungsten (W) impurity (inherent in the Mo precursor from the mining industry) was detected by XANES (see signal bumps for both 0.1Pt/α-MoC and 0.5Pt/α-MoC (dampened by more Pt). We note that the actual contributions by tungsten in both samples are almost identical (Table S2 by ICP, Figs. S11 by XPS, and XANES) but that the W counts in the XANES plots are normalized by Pt counts for each sample. By this, the tungsten signal in 0.5Pt/α-MoC is 5 times smaller when compared to 0.1Pt/α-MoC. Due to the overlap of W L_2 (~

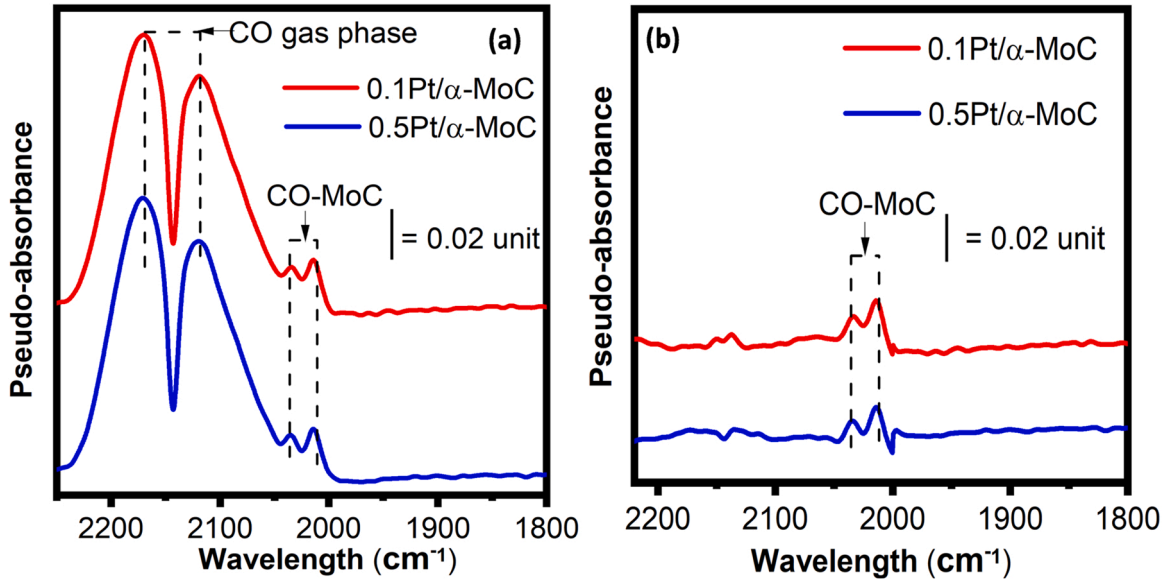

Fig. 6. CO-DRIFTS analyses of representative Pt/α-MoC catalysts: (a) CO-DRIFTS with CO in the feed stream for down-selected catalysts at 25 °C and (b) CO-DRIFT spectra for down-selected catalysts after CO gas phase subtraction from Fig. 6a.

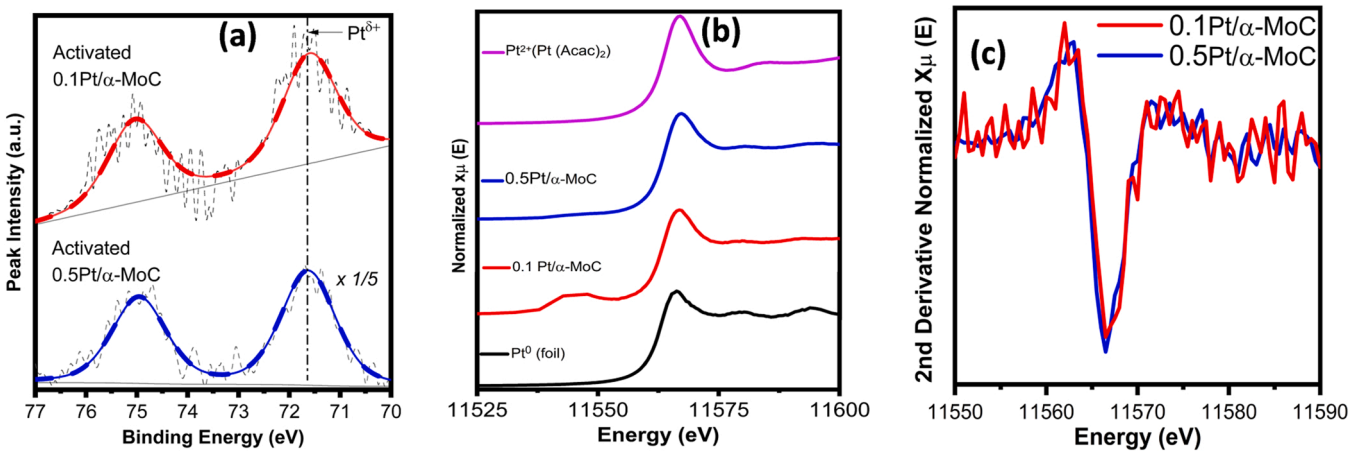

Fig. 7. X-ray characterizations of the local environment of Pt atoms as dilute single atoms and fully exposed ensembles: (a) In-situ XPS Pt *4 f* before reaction. (b) Normalized in-situ Pt *L3* XANES. The bump at ~ 11.54 keV (W *L2* edge) derives from an equal amount of W signal inherent in the MoC precursor. The bump of 0.5Pt/α-MoC is dampened due to the normalization of the W counts by Pt counts. (c) 2nd derivative normalized Pt *L3* XANES.

11.54 keV) and Pt L_3 (~11.56 keV) edges energy, the presence of the tungsten impedes us from performing reliable EXAFS analyses of the Pt-Mo coordination environment. Several efforts to obtain a W-free MoC precursor from various vendors within the USA were unsuccessful. Nevertheless, the presence of only 0.03 wt% of tungsten in the carbide supports (Table S2) and the reported much lower RWGS activity of tungsten carbides than molybdenum carbides [74] warrant the limited influence of the tungsten impurities on our overall findings.

As evidenced by the almost identical Pt footprints in 0.1Pt/α-MoC and 0.5Pt/α-MoC through CO-DRIFTS, XPS, and XANES studies, the Pt atoms of the fully exposed ensembles in 0.5Pt/α-MoC are still atomically dispersed Pt per se. Therefore, we hypothesize that, with the increases in the Pt loading, certain Pt-MoC catalytic functions may be blocked by these populated Pt atoms covering the catalytically active α-MoC substrates.

3.4. *Crowded Pt sites inhibit CO_2 activation at the critical Pt-Mo Interfaces of the interior Pt atoms*

To identify the possible compromised catalytic function(s) and the associated reaction intermediates at the crowded Pt-Mo sites, one would ideally map out the entire reaction pathways and every reaction intermediate involved in each elementary reaction step. This however seems to be a noble goal as the debate between redox and associative reaction (or their coexistence) pathways for CO_2 +H_2 reaction over MoC surfaces, with or without supported metals, is still ongoing [28,32,75,76]. We conducted DRIFTS under RWGS reaction (Fig. S12) for the 0.1Pt/α-MoC and 0.5Pt/α-MoC. At 250 °C, based on our reactor tests, we know there is an actual reaction taking place but did not capture any significant intermediates. But at 350 °C both formate species [28] (associative pathway intermediates) and CO gas (products) were detected. We however note that this is not adequate to conclude that the reaction follows the formate route. Otherwise, the formate should be significant at lower temperatures due to the more negative Gibbs free energy. Furthermore, it is also possible that the formate route observed at 350 °C (and not at 250 °C) is temperature-induced. Perhaps, at relatively lower temperatures (e.g., 250 °C), the reaction is predominantly by H_2-assisted direct CO_2 dissociation into CO and *OH [22] and/or direct dissociation of CO_2 while the formate route (associative) [28] becomes more substantial at elevated temperature (without necessarily excluding the redox pathway). In line with our RGWS-DRIFTS results, our kinetic studies (Fig. S13, SI-T2) were also unable to distinguish between the two classical RWGS reaction mechanisms. Nevertheless, critical reaction steps like H_2 adsorption/dissociation, C═O bond cleavage, and CO desorption are the general reaction steps that neither the redox nor associative reaction mechanism can circumvent. Therefore, we examined these steps to see which were compromised due to the presence of fully exposed Pt ensembles over the MoC substrate.

3.4.1. *Crowded Pt-centric site does not induce undesired -CO + -H interferences under RWGS-relevant conditions*

Although the CO-DRIFTS discussed earlier suggest that the α-MoC would be the predominant adsorption site for the CO under RWGS, tiny fractions of CO adsorption to the Pt-sites and its possible interference with the H_2 adsorption and activation would be our first suspected compromise. This is because while the adsorption energies govern the "easiness" of adsorptions and the site occupation equilibrium for various reaction intermediates at a given temperature,100% exclusion of certain adsorbates from a particular site is unlikely based on the concept of adsorption isotherm and adsorption competitions. Typically, in the range of 200–440 °C, strong adsorption of CO on supported metal (without necessarily poisoning the metal sites) in heterogeneous catalysts would lead to methanation instead of RWGS [24–26,77]. However, for our catalysts, the preference of having α-MoC rather than Pt as the binding site for CO (Fig. 6b) coupled with the overall facile desorption of CO from the MoC (Figs. S9 and S14) is not likely to interfere with H_2 adsorption and activation on the crowded single-atom Pt species. This is reflected by the invariant ~ 100% CO selectivity in RWGS reaction regardless of testing temperatures and CO_2/H_2 ratios (Figs. 2b and 8 a). We performed CO-H_2 pulse experiments to validate further the weak adsorption and low abundance of carbonyl species on the Pt-centric sites (Figs. 8b and 8c) under RWGS-relevant conditions. These net activities associated with the Pt-centric sites were obtained by subtracting the minor contributions of the bare MoC (Fig. S15) from the overall catalyst activities (Fig. S16). When CO+H_2 was introduced into the CO-preadsorbed catalyst (Fig. 8b), the adsorbed CO (due to adsorption isotherm, even in a tiny amount that cannot be seen in CO-DRIFTS) on the Pt-centric site would be displaced by H_2 but leaving ample room for a significant amount of CH_4 formation when *CO and *H are in adjacency, which is inconsistent with the actual reaction testing results. Contrastingly, when CO+H_2 was introduced to the H_2-preadsorbed catalyst, a minimal amount of CH_4 was produced (Fig. 8c), which agrees with the ~ 0% CH_4 selectivity in our RWGS tests, suggesting that the adsorption of *CO on Pt-centric site under actual reaction conditions is indeed minimal. In our actual RWGS conditions, CO would adsorb weakly on MoC and even more weakly on the Pt-centric sites, with H_2 almost completely overtaking the Pt-centric sites. The prominent role of the supported metal in activating H_2 was also noted for Au-MoC_x systems [27,78]. These comparisons suggest that, during the RWGS reaction, the formation and desorption of CO have minimal direct connections with the Pt

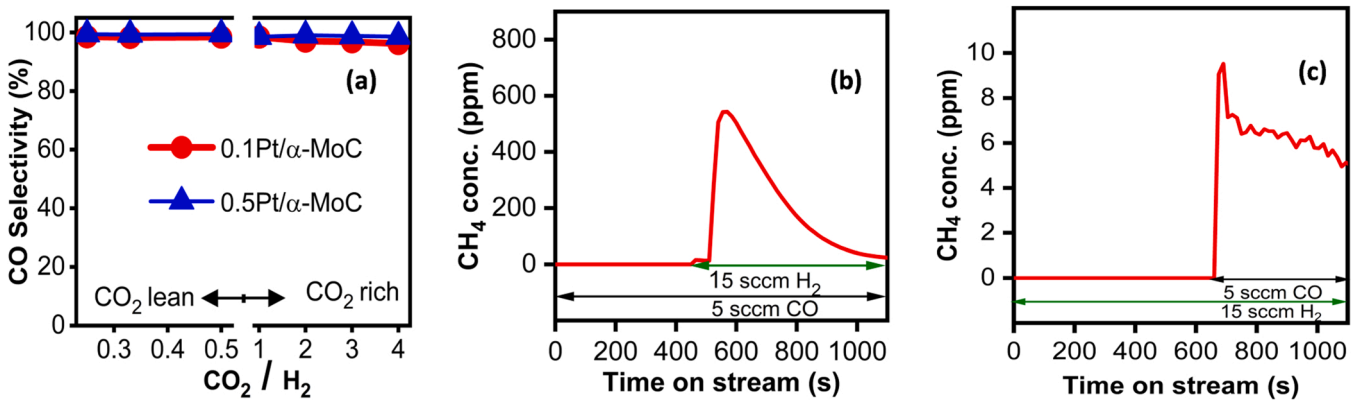

Fig. 8. CO/H2 pulse experiments reveal the substantially reduced opportunity for carbonyl and hydrogen species to coexist at the Pt-centric site to produce CH_4 under RWGS-relevant conditions: (a) RWGS CO selectivity as a function of CO_2/H_2 ratio at 250 °C (b) Pt-centric site methanation activity at 250 °C with CO-preadsorbed Pt/α-MoC after subtracting bulk α-MoC contribution and (c) Pt-centric site methanation activity at 250 °C with H_2-preadsorbed Pt/α-MoC after subtracting the much less-pronounced reactivity contributions from blank α-MoC.

site, but most likely take place on the MoC surfaces during the CO_2 activation. The Pt/ α-MoC catalysts are therefore an effective dual-site formulation, with Pt and α-MoC taking care of H_2 adsorption/activation and CO formation/ desorption respectively.

Although CO adsorption is weak, CO_2 can indeed still adsorb and get activated according to literature [29,30,40,79,80] and our CO_2-DRIFTS data (discussed later). Unlike the CO adsorbing linearly through its C-atom on molybdenum carbides (with the oxygen atom pointing away from the MoC), CO_2 still adsorbs via C-atom but binds in a bent configuration (molecular bond angle ~ 120–130°) with its oxygen atoms also adsorbed on the molybdenum carbides [40,81]. This bent geometry suggesting effective charge transfer from the molybdenum carbide to the CO_2 is accompanied by substantial elongation of the C═O bonds. Molybdenum carbides can rupture at least one of the C═O bonds of CO_2 and spontaneously release CO as product [27,31,81].

3.4.2. *Underutilization of crowded Pt-centric sites for CO_2 activation during RWGS*

The exclusion of any significant extent of undesired -CO + -H interferences associated with the crowded Pt-centric sites leads us to suspect that it was the CO_2 activation at the Pt-MoC interface that might have been impeded by the fully exposed Pt ensembles over the MoC substrate. We conducted in-situ XPS under the RWGS condition for 0.1Pt/α-MoC and 0.5Pt/α-MoC. Before the reaction, as shown earlier (Fig. 7a), both catalysts possessed the electron-deficient yet near-neutral Pt species ($Pt^{\delta+}$). However, from Fig. 9a, the Pt *4 f* XPS spectra acquired after 20 mins of reaction look different for the two samples. These reaction-quenched samples contained additional cationic Pt species, most likely Pt(II)-O, [73] which originate from the Pt site in contact with the deprived oxygen from the activated CO_2 [82,83]. The ratio of Pt(II): $Pt^{\delta+}$ for 0.1Pt/α-MoC is 42:58 (Table S3), indicating a statistically balanced distribution of catalytic centers where half of the Pt is associated with the oxygen-deprived from CO_2 (the remaining carbonyl species adsorbs on and desorbs from MoC as discussed earlier), and another half of the Pt has its associated oxygen consumed by the activated hydrogen and becomes ready for the next catalytic cycle. However, an unbalanced Pt(II):$Pt^{\delta+}$ ratio of 18:82 was recorded for 0.5Pt/α-MoC, suggesting that a substantial portion of its H_2-accessible Pt-Mo interfaces does not have access to the oxygen deprived from CO_2 activation (Fig. 9b & c).

We measured the reaction rate orders for CO_2 and H_2 at 250 °C for the 0.1 and 0.5Pt/α-MoC respectively (Fig. S13). The CO_2 rate order changed from 0.2 for 0.1Pt/α-MoC to 0.4 for 0.5Pt/α-MoC, while the H_2 rate order was largely the same or even slightly decreased: 0.3 for 0.1Pt/α-MoC and 0.2 for 0.5Pt/α-MoC. Based on the Langmuir-Hinshelwood reaction mechanism, the slight increase in surface coverage of H_2, if any, is signified by the slight decrease in the H_2 rate order from 0.1Pt/α-MoC to 0.5Pt/α-MoC. This suggests that the inadequate hydrogen

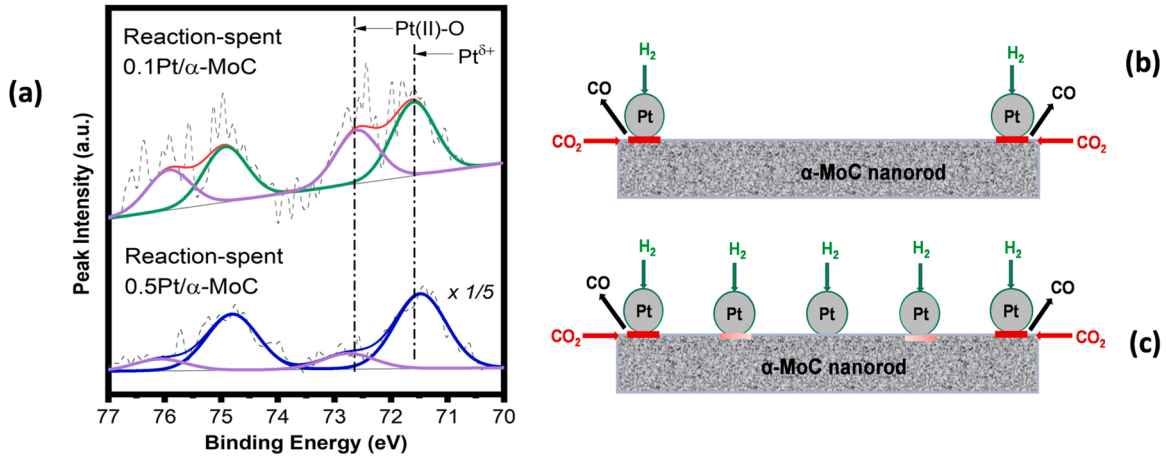

Fig. 9. Investigation of surface Pt population density effect on CO_2 activation at the Pt-Mo interface: (a) In-situ XPS Pt *4 f* spectra obtained after 20 mins RWGS at 250 °C. Schematics showing CO_2 activation at the Pt-Mo interface as a function of Pt surface population density: (b) unhindered CO_2 activation at the Pt-Mo interfaces in 0.1Pt/α-MoC and (c) hindered CO_2 activation at the Pt-Mo in 0.5Pt/α-MoC, where the crowded Pt atoms in the interior of the fully exposed Pt ensembles are underutilized during the CO_2 activation.

activation and subsequent water product removal would not be responsible for the decline in the intrinsic activity of the Pt-centric sites in 0.5Pt/α-MoC. Otherwise, this would adversely turn the Pt and Mo overly oxidized in the 0.5Pt/α-MoC when Pt atoms are underutilized, which is opposite to the actual XPS findings (Fig. 9 and S5).

Considering the molecule size of CO_2 (2.3 Å) against the tight spacing in the fully exposed Pt ensembles, we envision a substantial entropic barrier for CO_2 activation on the α-MoC when crowded Pt atoms are present to the top layer of the Pt-Mo interface. Although fully exposed, the Pt ensembles now behave in similar ways as quasi-nanoparticles or 2D raft [36], where a majority of the interior Pt-Mo in the ensembles become spectator species in CO_2 activation. This can be rationalized by the increased CO_2 rate order from 0.1Pt/α-MoC to 0.5Pt/α-MoC (Fig. S13), suggesting the Pt-Mo catalytic centers as a whole are experiencing a lower coverage of activated CO_2.

Nonetheless, the characteristic chemistry of our catalysts forbids us from interrogating the pertinent questions of possible differences in CO_2 adsorption and desorption behaviors on the representative catalysts, typically tractable with CO_2 temperature-programmed desorption experiment (SI-T3 challenges of TPD). Due to its oxophilic nature, surface oxidation of bare MoC by CO_2 at room temperature resulting from the adsorption and direct dissociation of CO_2 into carbon monoxide and oxygen has been reported [79]. The strong interaction of the leftover *O with the MoC will result in the carbide's surface-to-bulk oxidation, and its removal via heating will irreversibly destroy the catalyst [40,84–87]. Hence, the CO_2-TPD would become more of a temperature-programmed surface reaction, which is undesired. More so, to accurately evaluate the impact of the fully exposed Pt-centric site density on CO_2 adsorption and/or activation, the probe molecule (CO_2) would have to be precisely titrated against the Pt-centric sites with minimal interferences by the Pt-free α-MoC surfaces. However, these supported single-atom Pt species, at the loading of 0.1 and 0.5 wt%, occupy only a very small fraction of the α-MoC substrate. Our preliminary CO_2-DRIFTS data (Fig. S17) at 25–250 °C show that both catalysts display CO_2 adsorption in bent mode [88,89] on molybdenum carbide [90]. The identical CO_2 adsorption spectral signature for both loadings suggests no sensible difference(s) in CO_2 adsorption, perhaps as a result of the tiny amount of Pt-Mo catalytic centers in comparison to the vast majority of the blank α-MoC surfaces. There are no noticeable differences in terms of wavenumbers and peak symmetry even at 250 °C, suggesting that the contribution is overwhelmingly coming from the α-MoC surfaces instead of the critical Pt-Mo interfaces.

Furthermore, while the underutilization of Pt in the fully exposed ensembles, is the bottleneck problem toward high RWGS activity in this work, we declare it remains unclear whether the surface-doped Pt from 0.1 to 0.5 wt% would change the local activity of α-MoC, where the overall structural and valence properties of Mo was unchanged according to XRD and XPS analyses as discussed earlier. Searching for optimal structures of Pt to retain its own function while promoting the MoC activity would be an intriguing future direction.

4. Conclusion

Through the uniquely decoupled catalytic functions resulting from the interaction of the Pt and α-MoC, the Pt/α-MoC catalysts can deliver stable low-temperature RWGS activity via a bifunctional mechanism while forbidding the undesired methane formation. Despite the excellent catalytic performance of the Pt/α-MoC catalysts for RWGS, the higher surface density of atomically dispersed Pt species as ensembles adversely limits the intrinsic activity. These crowded surface Pt atoms on the MoC surfaces inhibit the function of Pt to serve as a transient site to take away the O during CO_2 activation on MoC, rendering the underutilization of the entire Pt-Mo moiety for efficient CO_2 activation. This caution is relevant to the design of supported metal catalysts for various reactions, especially when the supports serve as catalytically active ligands to activate reactants in concerto with the supported metals.

CRediT authorship contribution statement

Ewa Chukwu: Investigations (lead), formal data analysis and Visualisation, Writing – original draft, Writing – review & editing. **Lindsay Molina:** Investigation, Writing – review & editing - supporting. **Conner Rapp:** Investigation, Writing – review & editing - supporting. **Luis Morales:** Investigation, Writing – review & editing - supporting. **Zehua Jin**: Investigation, Writing – review & editing - supporting. **Stavros Karakalos:** Investigation (XPS), Writing – review & editing - supporting. **Hui Wang**: Investigation - microscopy, Writing – review & editing - supporting. **Sungsik Lee:** Investigation (XAS), Writing – review & editing - supporting. **Michael J. Zachmane**: Investigation - microscopy, Writing – review & editing - supporting. **Ming Yang:** Conceptualization, Funding acquisition, Project administration, Writing – review & editing.

Declaration of Competing Interest

The authors declare that they have no known competing financial interests or personal relationships that could have appeared to influence the work reported in this paper.

Data Availability

No data was used for the research described in the article.

Acknowledgment

M. Y. thanks the support provided by the start-up fund of Clemson University, the National Science Foundation Award 2146591, and American Chemical Society PRF Doctoral New Investigator Award 65606-DNI5. The use of 12-BM beamline of the Advanced Photon Source is supported by the U.S. Department of Energy (DOE) Office of Science User Facility operated for the DOE Office of Science by the Argonne National Laboratory under Contract No. DE-AC02–06CH11357. Post-reaction sample electron microscopy research was supported by the Center for Nanophase Materials Sciences (CNMS), which is a US Department of Energy, Office of Science User Facility at Oak Ridge National Laboratory. M.Y would like to use this research article to celebrate the retirement of William Coburn after 27 years of fantastic service to the Chemical Engineering Department of Clemson University.

Appendix A. Supporting information

Supplementary data associated with this article can be found in the online version at doi:10.1016/j.apcatb.2023.122532.

References

[1] S. Mitchell, J. Pérez-Ramírez, Atomically precise control in the design of low-nuclearity supported metal catalysts, Nat. Rev. Mater. 6 (2021) 969–985.
[2] A. Beniya, S. Higashi, Towards dense single-atom catalysts for future automotive applications, Nat. Catal. 2 (2019) 590–602.
[3] A.K. Datye, H. Guo, Single atom catalysis poised to transition from an academic curiosity to an industrially relevant technology, Nat. Commun. 12 (2021) 10–12.
[4] L. Liu, A. Corma, Metal catalysts for heterogeneous catalysis: from single atoms to nanoclusters and nanoparticles, Chem. Rev. 118 (2018) 4981–5079.
[5] X. Yang, A. Wang, B. Qiao, J.U.N. Li, Single-atom catalysts: a new, Frontier 46 (2013).
[6] M. Yang, et al., Catalytically active Au-O(OH)$_x$- species stabilized by alkali ions on zeolites and mesoporous oxides, Sci. (80). 346 (2014) 1498–1502.
[7] M. Yang, et al., A common single-site Pt(II)-O(OH)$_x$- species stabilized by sodium on 'active' and 'inert' supports catalyzes the water-gas shift reaction, J. Am. Chem. Soc. 137 (2015) 3470–3473.
[8] Ming Yang, et al., Atomically dispersed Au−(OH)$_x$ species bound on titania catalyze the low-temperature water-gas shift reaction, J. Am. Chem. Soc. 135 (2013) 3768–3771.
[9] F.D. Speck, et al., Atomistic insights into the stability of Pt single-atom electrocatalysts, J. Am. Chem. Soc. 142 (2020) 15496–15504.

[10] S. Jin, et al., A universal graphene quantum dot tethering design strategy to synthesize single-atom, in: Chemie- Int (Ed.), Catalysts. *Angew.*, 59, 2020, pp. 21885–21889.
[11] S. Cao, et al., Single-atom gold oxo-clusters prepared in alkaline solutions catalyse the heterogeneous methanol self-coupling reactions, Nat. Chem. 11 (2019) 1098–1105.
[12] H.V. Thang, G. Pacchioni, L. DeRita, P. Christopher, Nature of stable single atom Pt catalysts dispersed on anatase TiO_2, J. Catal. 367 (2018) 104–114.
[13] L. DeRita, et al., Structural evolution of atomically dispersed Pt catalysts dictates reactivity, Nat. Mater. 18 (2019) 746–751.
[14] L. DeRita, et al., Catalyst architecture for stable single atom dispersion enables site-specific spectroscopic and reactivity measurements of CO adsorbed to Pt atoms, oxidized Pt clusters, and metallic Pt clusters on TiO_2, J. Am. Chem. Soc. 139 (2017) 14150–14165.
[15] J.D. Kistler, et al., A single-site platinum CO oxidation catalyst in zeolite KLTL: microscopic and spectroscopic determination of the locations of the platinum atoms, Angew. Chem. Int. Ed. 53 (2014) 8904–8907.
[16] J. Guzman, B.C. Gates, Structure and reactivity of a mononuclear gold- complex catalyst supported on magnesium oxide, Angew. Chem. Int. Ed. 115 (6) (2003) 714–717.
[17] M.D. Marcinkowski, et al., Pt/Cu single-atom alloys as coke-resistant catalysts for efficient C-H activation, Nat. Chem. 10 (2018) 325–332.
[18] F.R. Lucci, et al., Selective hydrogenation of 1,3-butadiene on platinum-copper alloys at the single-atom limit, Nat. Commun. 6 (2015) 1–8.
[19] X. Hai, et al., Scalable two-step annealing method for preparing ultra-high-density single-atom catalyst libraries, Nat. Nanotechnol. 17 (2022) 174–181.
[20] A. Mehmood, et al., High loading of single atomic iron sites in Fe–NC oxygen reduction catalysts for proton exchange membrane fuel cells, Nat. Catal. 5 (2022) 311–323.
[21] C. Xia, et al., General synthesis of single-atom catalysts with high metal loading using graphene quantum dots, Nat. Chem. 13 (2021) 887–894.
[22] J. Zheng, et al., High loading of transition metal single atoms on chalcogenide catalysts, J. Am. Chem. Soc. 143 (2021) 7979–7990.
[23] M. Chen, D. Kumar, C.W. Yi, D.W. Goodman, Chemistry: the promotional effect of gold in catalysis by palladium-gold, Science (80) 310 (2005) 291–293.
[24] J.C. Matsubu, V.N. Yang, P. Christopher, Isolated metal active site concentration and stability control catalytic CO_2 reduction selectivity, J. Am. Chem. Soc. 137 (2015) 3076–3084.
[25] X. Chen, et al., Theoretical insights and the corresponding construction of supported metal catalysts for highly selective CO_2 to CO conversion, ACS Catal. 7 (2017) 4613–4620.
[26] A. Aitbekova, et al., Low-temperature restructuring of CeO_2-supported ru nanoparticles determines selectivity in CO_2 catalytic reduction, J. Am. Chem. Soc. 140 (2018) 13736–13745.
[27] M. Figueras, et al., Supported molybdenum carbide nanoparticles as an excellent catalyst for CO_2 hydrogenation, ACS Catal. 11 (2021) 9679–9687.
[28] X. Zhang, et al., Synergy between β-Mo_2C nanorods and non-thermal plasma for selective CO_2 reduction to CO, Chem 6 (2020) 3312–3328.
[29] X. Liu, et al., Effective and highly selective CO generation from CO_2 using a polycrystalline α-Mo_2C catalyst, ACS Catal. 7 (2017) 4323–4335.
[30] X. Zhang, et al., Highly dispersed copper over β-Mo_2C as an efficient and stable catalyst for the reverse water gas shift (RWGS) reaction, ACS Catal. 7 (2017) 912–918.
[31] S. Posada-Pérez, et al., Highly active Au/δ-MoC and Cu/δ-MoC catalysts for the conversion of CO_2: the Metal/C ratio as a key factor defining activity, selectivity, and stability, J. Am. Chem. Soc. 138 (2016) 8269–8278.
[32] M.D. Porosoff, X. Yang, J.A. Boscoboinik, J.G. Chen, Molybdenum carbide as alternative catalysts to precious metals for highly selective reduction of CO_2 to CO, Angew. Chem. Int. Ed. 53 (2014) 6705–6709.
[33] R. Michalsky, Y.J. Zhang, A.J. Medford, A.A. Peterson, Departures from the adsorption energy scaling relations for metal carbide catalysts, J. Phys. Chem. C. 118 (2014) 13026–13034.
[34] L.L. Jewell, B.H. Davis, Review of absorption and adsorption in the hydrogen-palladium system, Appl. Catal. A Gen. 310 (2006) 1–15.
[35] J. Liu, et al., Tackling CO poisoning with single-atom alloy catalysts, J. Am. Chem. Soc. 138 (2016) 6396–6399.
[36] L.T. Thompson, J. Schaidle, N. Schweitzer, High activity carbide supported catalysts for water gas shift, J. Am. Chem. Soc. 133 (2011) 2378–2381.
[37] K.D. Sabnis, et al., Water-gas shift catalysis over transition metals supported on molybdenum carbide, J. Catal. 331 (2015) 162–171.
[38] J.S. Chen, Y.L. Cheah, S. Madhavi, X.W. Lou, Fast synthesis of α-MoO_3 nanorods with controlled aspect ratios and their enhanced lithium storage capabilities, J. Phys. Chem. C. 114 (2010) 8675–8678.
[39] B.M. Wyvratt, J.R. Gaudet, L.T. Thompson, Effects of passivation on synthesis, structure and composition of molybdenum carbide supported platinum water-gas shift catalysts, J. Catal. 330 (2015) 280–287.
[40] S. Posada-Pérez, et al., The bending machine: CO_2 activation and hydrogenation on δ-MoC(001) and β-Mo_2C(001) surfaces, Phys. Chem. Chem. Phys. 16 (2014) 14912–14921.
[41] C. Kunkel, F. Viñes, F. Illas, Transition metal carbides as novel materials for CO_2 capture, storage, and activation, Energy Environ. Sci. 9 (2016) 141–144.
[42] A. Álvarez, et al., CO_2 activation over catalytic surfaces, ChemPhysChem 18 (2017) 3135–3141.
[43] F. Maurer, et al., Tracking the formation, fate and consequence for catalytic activity of Pt single sites on CeO_2, Nat. Catal. 3 (2020) 824–833.
[44] H. Wang, et al., Surpassing the single-atom catalytic activity limit through paired Pt-O-Pt ensemble built from isolated Pt_1 atoms, Nat. Commun. 10 (2019) 1–12.
[45] X. Zhang, et al., A stable low-temperature H_2-production catalyst by crowding Pt on α-MoC, Nature 589 (2021) 396–401.
[46] L. Lin, et al., A highly CO-tolerant atomically dispersed Pt catalyst for chemoselective hydrogenation, Nat. Nanotechnol. 14 (2019) 354–361.
[47] F. Cai, et al., Low-temperature hydrogen production from methanol steam reforming on Zn-modified Pt/MoC catalysts, Appl. Catal. B Environ. 264 (2020).
[48] L. Lin, et al., Low-temperature hydrogen production from water and methanol using Pt/α-MoC catalysts, Nature 544 (2017) 80–83.
[49] L. Liu, Q. Guo, Isokinetic relationship, isoequilibrium relationship, and enthalpy – entropy compensation, Chem. Rev. 101 (2001) 673–695.
[50] J.A. Byers, T.F. Jamison, Entropic factors provide unusual reactivity and selectivity in epoxide-opening reactions promoted by water, Proc. Natl. Acad. Sci. U. S. A. 110 (2013) 16724–16729.
[51] M. Tamura, K. Sawabe, K. Tomishige, A. Satsuma, K.I. Shimizu, Substrate-specific heterogeneous catalysis of CeO2 by entropic effects via multiple interactions, ACS Catal. 5 (2015) 20–26.
[52] M. Guo, et al., Enthalpy-entropy compensation effect in oxidation reactions by manganese(IV)-oxo porphyrins and nonheme iron(IV)-oxo models, J. Am. Chem. Soc. 143 (2021) 18559–18570.
[53] J. Zhang, et al., Importance of species heterogeneity in supported metal catalysts, J. Am. Chem. Soc. 144 (2022) 5108–5115.
[54] Z. Liu, et al., Tuning the selectivity of catalytic nitriles hydrogenation by structure regulation in atomically dispersed Pd catalysts, Nat. Commun. 12 (2021) 1–8.
[55] C. Dong, et al., Fully exposed palladium cluster catalysts enable hydrogen production from nitrogen heterocycles, Nat. Catal. 5 (2022) 485–493.
[56] J. Guo, et al., Kinetic evidence of most abundant surface intermediates variation over Ptnand Ptp: few-atom Pt ensembles enable efficient catalytic cyclohexane dehydrogenation for hydrogen production-II, ACS Catal. (2022) 7248–7261, https://doi.org/10.1021/acscatal.2c01420.
[57] Y. Deng, et al., Few-atom Pt ensembles enable efficient catalytic cyclohexane dehydrogenation for hydrogen production, J. Am. Chem. Soc. 144 (2022) 3535–3542.
[58] H. Jeong, et al., Highly durable metal ensemble catalysts with full dispersion for automotive applications beyond single-atom catalysts, Nat. Catal. 3 (2020).
[59] H. Jeong, et al., Fully dispersed Rh ensemble catalyst to enhance low-temperature activity, J. Am. Chem. Soc. 140 (2018) 9558–9565.
[60] S. Yao, et al., Atomic-layered Au clusters on α-MoC as catalysts for the low-temperature water-gas shift reaction, Science 357 (2017) 389–393, https://doi.org/10.1126/science.aah4321.
[61] Y. Ma, et al., High-density and thermally stable palladium single-atom catalysts for chemoselective hydrogenations, Angew. Chem. Int. Ed. 59 (2020) 21613–21619.
[62] Y. Tang, et al., Rh single atoms on TiO_2 dynamically respond to reaction conditions by adapting their site, Nat. Commun. 10 (2019) 1–10.
[63] L. Nie, et al., Activation of surface lattice oxygen in single-atom Pt/CeO_2 for low-temperature CO oxidation, *Sci. (80).* 358 (2017) 1419–1423.
[64] B. Qiao, et al., Single-atom catalysis of CO oxidation using Pt_1/FeO_x, Nat. Chem. 3 (2011) 634–641.
[65] H. Li, et al., Synergetic interaction between neighbouring platinum monomers in CO_2 hydrogenation, Nat. Nanotechnol. 13 (2018) 411–417.
[66] J. Li, et al., Highly active and stable metal single-atom catalysts achieved by strong electronic metal-support interactions, J. Am. Chem. Soc. 141 (2019) 14515–14519.
[67] L. DeRita, et al., Catalyst architecture for stable single atom dispersion enables site-specific spectroscopic and reactivity measurements of CO adsorbed to Pt atoms, oxidized Pt clusters, and metallic Pt clusters on TiO_2, J. Am. Chem. Soc. 139 (2017) 14150–14165.
[68] W. Tan, et al., Tuning single-atom Pt_1−CeO_2 catalyst for efficient CO and C3H6 oxidation: size effect of ceria on Pt structural evolution, ChemNanoMat (2020) 1797–1805, https://doi.org/10.1002/cnma.202000431.
[69] X.I. Pereira-Hernández, et al., Tuning Pt-CeO_2 interactions by high-temperature vapor-phase synthesis for improved reducibility of lattice oxygen, Nat. Commun. 10 (2019).
[70] A. Paredes-Nunez, I. Jbir, D. Bianchi, F.C. Meunier, Spectrum baseline artefacts and correction of gas-phase species signal during diffuse reflectance FT-IR analyses of catalysts at variable temperatures, Appl. Catal. A Gen. 495 (2015) 17–22.
[71] H. Shou, L. Li, D. Ferrari, D.S. Sholl, R.J. Davis, Use of infrared spectroscopy and density functional theory to study the influence of rubidium on alumina-supported molybdenum carbide catalyst for higher alcohol synthesis from syngas, J. Catal. 299 (2013) 150–161.
[72] M.L. Colaianni, J.G. Chen, W.H. Weinberg, J.T. Yates, The adsorption and dissociation of carbon monoxide on clean and oxygen-modified Mo(110) surfaces, J. Am. Chem. Soc. 114 (1992) 3735–3743.
[73] Retrieved: 05/ 2023 01/.⟨https://www.thermofisher.com/us/en/home/materials-science/learning-center/periodic-table/transition-metal/platinum.html⟩.
[74] J.R. Morse, M. Juneau, J.W. Baldwin, M.D. Porosoff, H.D. Willauer, Alkali promoted tungsten carbide as a selective catalyst for the reverse water gas shift reaction, J. CO_2 Util. 35 (2020) 38–46.
[75] J. Gao, et al., Controllable synthesis of α-MoC1-x and β-Mo2C nanowires for highly selective CO_2 reduction to CO, Catal. Commun. 84 (2016) 147–150.
[76] K.P. Reddy, et al., Molybdenum carbide catalyst for the reduction of CO_2 to CO: surface science aspects by NAPPES and catalysis studies, Dalt. Trans. 48 (2019) 12199–12209.
[77] A.S. Li, et al., Tuning the CO_2 hydrogenation selectivity of rhodium single-atom catalysts on zirconium dioxide with alkali ions, Angew. Chem. (2022), https://doi.org/10.1002/ange.202218167.

[78] E. Florez, T. Gomez, J.A. Rodriguez, F. Illas, On the dissociation of molecular hydrogen by Au supported on transition metal carbides: Choice of the most active support, Phys. Chem. Chem. Phys. 13 (2011) 6865–6871.
[79] W. Wu, et al., An IR study on the surface passivation of Mo_2C/Al_2O_3 catalyst with O_2,H_2O and, Phys. Chem. Chem. Phys. 5603–5608 (2004) CO_2.
[80] Q. Zhang, L. Pastor-Pérez, W. Jin, S. Gu, T.R. Reina, Understanding the promoter effect of Cu and Cs over highly effective B-Mo_2C catalysts for the reverse water-gas shift reaction, Appl. Catal. B Environ. 244 (2019) 889–898.
[81] S. Posada-Pérez, F. Viñes, J.A. Rodriguez, F. Illas, Fundamentals of methanol synthesis on metal carbide based catalysts: activation of CO_2 and H2, Top. Catal. 58 (2015) 159–173.
[82] S.S. Kim, H.H. Lee, S.C. Hong, A study on the effect of support's reducibility on the reverse water-gas shift reaction over Pt catalysts, Appl. Catal. A Gen. 423–424 (2012) 100–107.
[83] Y. Li, et al., Dynamic structure of active sites in ceria-supported Pt catalysts for the water gas shift reaction, Nat. Commun. 12 (2021) 1–9.
[84] A. Mehdad, R.E. Jentoft, F.C. Jentoft, Passivation agents and conditions for Mo_2C and W_2C: effect on catalytic activity for toluene hydrogenation, J. Catal. 347 (2017) 89–101.
[85] T. Mo, J. Xu, Y. Yang, Y. Li, Effect of carburization protocols on molybdenum carbide synthesis and study on its performance in CO hydrogenation, Catal. Today 261 (2016) 101–115.
[86] K.J. Leary, J.N. Michaels, A.M. Stacy, Carbon and oxygen atom mobility during activation of Mo_2C catalysts, J. Catal. 101 (1986) 301–313.
[87] (St) T.P. Clair, S.T. Oyama, D.F. Cox, CO and O_2 adsorption on α-Mo2C (0001), Surf. Sci. 468 (2000) 62–76.
[88] X. Zhang, S.P. Sander, Infrared absorption spectra of the CO_2/H_2O complex in a cryogenic nitrogen matrix-detection of a new bending frequency, J. Phys. Chem. A 115 (2011) 9854–9860.
[89] D. Dos Santos Silva, A.E.C. Villegas, R.D.F. Bonfim, V.M.M. Salim, N.S. De Resende, Iron-substituted hydroxyapatite as a potential photocatalyst for selective reduction of CO_2 with H2, J. CO_2 Util. 63 (2022), 102102.
[90] Gamp,S. Vibrational Spectra of Carbon Dioxide and Carbon Disulfide. (2022). https://www.d.umn.edu/~psiders/courses/chem4644/reportGuide/CO2CS2sampleReportRetrieved: 07/01/2023.